Ninth International Conference on CFD in the Minerals and Process Industries
CSIRO, Melbourne, Australia
10–12 December 2012

FORCES ARISING DURING BUBBLE–PARTICLE INTERACTION

David I. VERRELLI[1*], Andrew LEE[1,3], M. Philip SCHWARZ[2] and Peter T. L. KOH[2]

[1] CSIRO Process Science and Engineering, Clayton, Victoria 3168, AUSTRALIA
[2] CSIRO Mathematics, Informatics and Statistics, Clayton, Victoria 3168, AUSTRALIA
[3] Chemical and Biomolecular Engineering, The University of Melbourne, Victoria 3010, AUSTRALIA
*Corresponding author, E-mail address: David.Verrelli@csiro.au

ABSTRACT

In numerous natural and industrial situations, including froth flotation, particles and bubbles interact, and sometimes attachment is achieved.

Through direct experimental observation of a particle dropping onto a stationary bubble, we have described particle–bubble interaction and attachment at low Reynolds numbers. Increased understanding can be gained by comparison to numerical modelling predictions.

Our modelling incorporated:

- Stokes drag;
- inertia and added mass;
- buoyancy; and
- microhydrodynamic resistances, due to flow of liquid between the bubble and the approaching or retracting particle.

The governing differential equation was resolved into radial and tangential components, and solved numerically to produce predictions of particle trajectories, and velocities, which can be used to predict the likelihood of attachment, and the 'induction period' for attachment. These can be compared to the experimental results.

Even greater insight is obtained by explicitly evaluating the force components. The evolution of these forces over time reveals which mechanism is controlling the interaction at various stages. It also provides a basis for inclusion or neglect of other terms in the governing equation (*e.g.* Basset force).

We simulated the interaction for a variety of approach trajectories, with different particle densities. We also simulated cases in which particles approach at elevated speeds, as could occur in a real system where particles are accelerated by turbulent eddies toward a bubble that is enveloped by a laminar boundary layer.

We found that increasing the initial velocity does not necessarily decrease the induction period, as deceleration can occur rapidly, before the particle is very close to the bubble. Particles impinging on the bubble away from the bubble's apex exhibited longer induction periods.

If a repulsion of chemical origin prevents attachment, then low-energy particles 'slide' off the bubble, while high-energy particles could 'bounce' off the bubble's surface.

NOMENCLATURE

C_i	coefficients in approximate formula for f_r
D_i	coefficients in approximate formula for f_t
f_i	corrections to radial (i=r) or tangential (i=t) drag for microhydrodynamic effects, assuming no-slip boundary conditions
$F_{i,j}$	radial (i=r) or tangential (i=t) force components: inertia and added mass (j=IAM); Stokes drag (j=Stokes); microhydrodynamic drag (j=MHD); buoyancy (j=grav)
$\boldsymbol{g}$	gravitational acceleration
m_i	mass of particle (i=p) or fluid displaced by particle (i=f)
m_*	$= m_p + m_f/2$
N_{Re}	Reynolds number
r	radial position of particle centre
R_b	bubble radius
R_p	particle radius
s	ratio of particle release velocity to Stokes settling velocity
t	time
t_{ind}	induction period for particle–bubble attachment
t_{slide}	duration of sliding by particle on bubble's surface
$\boldsymbol{v}_i$	velocity in the i-direction
$\boldsymbol{v}_S$	Stokes velocity
δ	gap, the shortest distance between particle and bubble surfaces
δ_{crit}	gap at which hard-sphere repulsion becomes important
Δ	hard-sphere repulsion term
ε	dimensionless gap, δ/R_p
μ	dynamic viscosity
ρ_i	density of particle (i=p) or fluid (i=f)
τ	parameter related to the viscous relaxation time
φ	polar angle of particle centre, measured from vertical

INTRODUCTION

The mechanism of flotation and its ability to serve as a cost effective and convenient separating process has resulted in it being used extensively within the mining, minerals and wastewater treatment industries. It has been estimated that flotation is used to process around 85 % of coal and minerals mined annually (Nguyen & Schulze, 2004).

Mineral particles in suspension interact with air bubbles that are introduced by various means. The key to

successful froth flotation is the selective formation of attachments between bubbles and certain classes of particle. At very close range, the surface chemistries of the particles and bubbles are important. However, the hydrodynamics of the interaction controls the opportunity for attachment, inasmuch as even favourable chemistry will count for nought if the particle and bubble cannot be brought sufficiently close together.

Traditionally this 'opportunity for attachment' is characterised in terms of the duration of particle sliding over the bubble's surface, t_{slide} (Nguyen & Schulze, 2004; Verrelli *et al.*, 2011). This concept is based on the observation that prior to attachment a particle is seen to slide around the circumference of a bubble, with a small gap — invisible to the naked eye — between the two objects' surfaces.

The sliding duration is then compared against a threshold induction period, t_{ind}, which is defined as the time to achieve attachment once a 'sliding' interaction has commenced (Sven-Nilsson, 1934; Verrelli *et al.*, 2011). Although conventionally the induction period is tacitly regarded as a constant, recent results from experimental observation and numerical modelling (Verrelli *et al.*, 2012b) indicate that it can vary depending on the orientation of the particle's approach trajectory with respect to the bubble.

Experimentally the induction period has been directly determined by monitoring individual particle positions as they interact with a stationary bubble (Verrelli & Koh, 2010; Verrelli *et al.*, 2011). The premise for this is illustrated in **Figure 1**. After settling more-or-less freely, one particle is seen to slide briefly at approximately constant radial position and then withdraws, while the other particle slides for longer and manifests an abrupt 'jump' in toward the bubble, signifying attachment. The induction period can be obtained directly for particle b.

In the present work we delve deeper into the numerical model, to determine the separate contributions of each major component to the radial and tangential forces acting upon the particle. Such analysis is helpful immediately in allowing greater understanding of the particle–bubble interaction in general, and specifically in interpreting the variation of induction period with particle trajectory. It also provides a useful basis for determining the importance of other terms that could be added to the governing equation. Finally, the work can serve as a foundation for greater understanding of analogous interactions that occur in numerous other natural and industrial operations, such as particle–particle interactions in coagulation, fluidisation, and jigging.

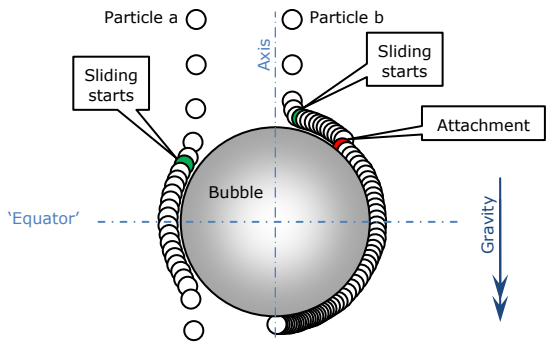

Figure 1: (a) A particle that slides briefly but does not attach. (b) A particle that slides for longer, and attaches.

MODEL DESCRIPTION

Scenario

The numerical model was set up to emulate the *CSIRO Milli-Timer* apparatus (Verrelli & Koh, 2010; Verrelli *et al.*, 2011), in which a particle falls under the influence of gravity through a quiescent medium onto a stationary bubble (as in **Figure 1**). However, it has been extended to describe the case in which the particles have been accelerated above Stokes velocity upon their approach to the bubble. Although particles may originate a large distance away from the bubble, presently we consider only the motion commencing from an initial position 1 mm away. It may be noted that this distance is approximately equal to the boundary layer that can be expected in a turbulent flow environment (Liu & Schwarz, 2009), and so the present results can give broader insight for a variety of flow regimes in the bulk.

The particles are presently considered to be perfect spheres, of diameter 150 µm. (Other shapes have been considered experimentally (Verrelli *et al.*, 2012a), but are not practical to model for current purposes.) The bubble is taken to be a rigid sphere with a no-slip boundary condition, with a diameter of 1.30 mm. (Modelling of bubbles with a slip boundary condition was presented by Verrelli *et al.* (2011); a hybrid boundary condition is discussed in a companion paper (Verrelli, 2012).) Both particle and bubble dimensions are within the range of sizes typically encountered in industrial operations (Newcombe, 2009).

The fluid is water, with nominal density of 1000 kg/m^3 and viscosity of 1 mPa.s. Industrial flotation cells commonly operate at somewhat elevated temperatures, in which case the viscosity would be reduced.

The particles are modelled with two different densities: 2450 kg/m^3, representing glass or silica, and 7600 kg/m^3, representing galena. The different densities yield different velocities and kinetic energies on approach, and provide an indication of particle inertia effects.

The particles are released at varying distances away from the vertical axis passing through the bubble's centre. Moreover, varying release velocities are investigated, emulating the effects of more vigorous interactions in a flotation cell, due to rapid rise of the bubble, particle swarm effects, or turbulent eddies transporting the particles. The release velocity is quantified in terms of a multiple, s, of the Stokes settling velocity.

Particle sliding is specified to commence once the gap decreases to 1 µm, while nominal attachment is specified at a gap of 10 nm, consistent with our previous work (Verrelli *et al.*, 2012b).

To permit consideration of the trajectories of particles that do not attach, *e.g.* due to mutually repulsive surface chemistry effects, the predicted path of the particle continues beyond the nominal attachment, albeit that the gap is constrained never to reduce significantly below 1 nm.

The various important gaps are summarised in **Table 1**.

Gap, δ [mm]	Meaning
1	Initial separation
0.001	Sliding commences
0.00001	Attachment occurs
0.000001	Minimum value (approximate)

Table 1: Important gaps and their meanings.

Numerical modelling

The numerical model employed presently is adapted from that described previously (Verrelli *et al.*, 2011) to predict particle trajectories; the independent variables of δ (or r) and φ track the particle's centre.

The governing equations are obtained from the Basset–Boussinesq–Oseen (BBO) equation (Nguyen & Schulze, 2004), neglecting the Basset force. A system of four equations is obtained:

$$\frac{\mathrm{d}v_\delta}{\mathrm{d}t} = \frac{{v_\varphi}^2}{r} - \frac{f_\mathrm{r}\, v_\delta + v_\mathrm{S}\cos\varphi}{\tau} + \Delta\,, \tag{1a}$$

$$\frac{\mathrm{d}v_\varphi}{\mathrm{d}t} = -\frac{v_\delta\, v_\varphi}{r} - \frac{f_\mathrm{t}\, v_\varphi - v_\mathrm{S}\sin\varphi}{\tau}\,, \tag{1b}$$

$$\frac{\mathrm{d}\delta}{\mathrm{d}t} = v_\delta \quad = v_r\,, \tag{1c}$$

$$\frac{\mathrm{d}\varphi}{\mathrm{d}t} = \frac{v_\varphi}{r} \tag{1d}$$

in which

$$r = R_\mathrm{b} + \delta + R_\mathrm{p}\,, \tag{2}$$

$$\tau \equiv \frac{{R_\mathrm{p}}^2\left(2\rho_\mathrm{p} + \rho_\mathrm{f}\right)}{9\mu}\,, \tag{3}$$

$$\boldsymbol{v}_\mathrm{S} \equiv \frac{2{R_\mathrm{p}}^2\left(\rho_\mathrm{p} - \rho_\mathrm{f}\right)}{9\mu}\boldsymbol{g}\,, \tag{4}$$

$$\Delta = \left(\frac{\delta_\mathrm{crit}}{\delta}\right)^{200}\,. \tag{5}$$

We have made several notable changes to the equations and their solution since the previously described work.

(i) The independent variable has been changed from r to δ, to reduce truncation errors.

(ii) The formulæ for the drag correction functions f_r and f_t have been improved to yield improved accuracy, without being too computationally expensive, in the respective forms

$$f_\mathrm{r} = \left[1 + \frac{1}{\varepsilon^{12}} + \sum_{n=1}^{11}\frac{C_n}{\varepsilon^n}\right]^{1/12}\,, \tag{6}$$

$$f_\mathrm{t} = 1 + D_1\left[\ln\left(1 + \sum_{n=1}^{4}\frac{D_{n+1}}{\varepsilon^n}\right)\right]^{D_6}\,. \tag{7}$$

These approximation formulæ were inspired by others in the literature (Chaoui & Feuillebois, 2003; Nguyen & Evans, 2004; Nguyen & Schulze, 2004). The coefficients were determined by nonlinear optimisation in *MATLAB* to reduce the sum of squares of errors in the logarithms of the values, for a range of dimensionless gaps from 10^{-10} to 10^{+3}, logarithmically spaced. For f_r the approximation was fit to the 'exact' values (Nguyen & Schulze, 2004); for f_t the highly accurate expressions of Chaoui & Feuillebois (2003) were used; note that f_t is specified for the case of zero nett torque, and is obtained from a combination of four elementary resistance functions (Nguyen & Schulze, 2004). With these changes the accuracy of the drag correction functions has improved from better than ±4 % and ±0.2 % (radial and tangential) to better than ±0.04 % and ±0.02 %. For values of C_i and D_i see the Appendix.

(iii) The governing system of equations was found to constitute a 'stiff system' whenever the predicted particle trajectory encountered small gaps, for which the microhydrodynamic resistances increased sharply. Hence greatly improved computational efficiency was obtained by swapping from a Runge–Kutta algorithm to a variable-order solver (implemented at order 5), based on numerical differentiation formulæ, that is well-suited to stiff problems — namely the `ode15s` routine in *MATLAB* (Shampine & Reichelt, 1997).

(iv) Tolerances in solving the differential equations were tightened. The solution components were required to achieve a fractional error of approximately 2×10^{-14} for all components greater than 1×10^{-14} in magnitude.

(v) A hard-sphere repulsion has been introduced to avoid physically implausible gaps of less than atomic dimensions (or even negative values); δ_crit is set to 1 nm. It is beyond the scope of the present work to investigate specific forms of Δ, and we do not claim equation 5 to represent the exact response. (Without this repulsion term the vanishingly small nominal gap will yield very large values of f_r and f_t, which may approximate the increase that actually occurs due to deformation of the bubble surface that is not modelled.) It must be emphasised that this term only affects the trajectories of particles after attachment is predicted to have occurred given favourable chemistry, and hence approximates the behaviour in the case of unfavourable chemistry when attachment is precluded.

(vi) The arguments of f_r and f_t were not altered for small gaps, less than 10 nm.

Analysis

Cases

Four cases are examined, as per **Table 2**.

Case	ρ_p [kg/m^3]	s [–]	Initial N_Re [–]
A	2450	1	6.5
B	2450	4	26
C	7600	1	92
D	7600	4	369

Table 2: Cases modelled.

Trajectories

Three trajectories are examined closely in each case, corresponding to starting positions given in **Table 3**. These correspond to particles that approach almost the bubble's apex, midway between the apex and edge, and just at the edge of the bubble. The trajectories are illustrated in the Results section.

Trajectory	Initial offset from vertical axis [mm]
a	0.100
b	0.400
c	0.700

Table 3: Trajectories that are discussed in detail herein.

Force components

For each trajectory, the governing equations are decomposed to identify four separate contributions radially, and four tangentially. That is,

$$0 = F_{i,\mathrm{IAM}} + F_{i,\mathrm{Stokes}} + F_{i,\mathrm{MHD}} + F_{i,\mathrm{grav}} + \Delta\,, \quad (8)$$

in which i=r or i=t, for radial or tangential terms. The hard-sphere term is not shown below, but can be obtained by difference.

The individual force components are evaluated as per **Table 4**.

Force	Radial component	Tangential component
Inertia and added mass, $F_{i,\mathrm{IAM}}$	$-m_* \left(\frac{\mathrm{d}v_\delta}{\mathrm{d}t} - \frac{{v_\varphi}^2}{r} \right)$	$-m_* \left(\frac{\mathrm{d}v_\varphi}{\mathrm{d}t} + \frac{v_\delta\, v_\varphi}{r} \right)$
Stokes drag, $F_{i,\mathrm{Stokes}}$	$-6\,\pi\,\mu\,R_\mathrm{p}\,v_\delta$	$-6\,\pi\,\mu\,R_\mathrm{p}\,v_\varphi$
Microhydro-dynamic drag, $F_{i,\mathrm{MHD}}$	$-(f_\mathrm{r}-1)\,6\,\pi\,\mu\,R_\mathrm{p}\,v_\delta$	$-(f_\mathrm{t}-1)\,6\,\pi\,\mu\,R_\mathrm{p}\,v_\varphi$
Buoyancy, $F_{i,\mathrm{grav}}$	$-(m_\mathrm{p}-m_\mathrm{f})\,g\cos(\varphi)$	$+(m_\mathrm{p}-m_\mathrm{f})\,g\sin(\varphi)$

Table 4: Formulæ for force components.

RESULTS

Trajectories

The trajectories for each case are shown in **Figure 2**. The three trajectories identified in **Table 3** are shown in darker, bolder lines. The trajectories track the centre of a given particle.

It is interesting to observe 'bouncing' in the case of the most energetic particles, at a density of 7600 kg/m^3 and initial velocity 4 times greater than v_S (case D). Such interactions were experimentally observed by Schulze & Gottschalk (1981), and have also been seen in our own laboratory with particles impacting at high velocity, illustrated in **Figure 3**.

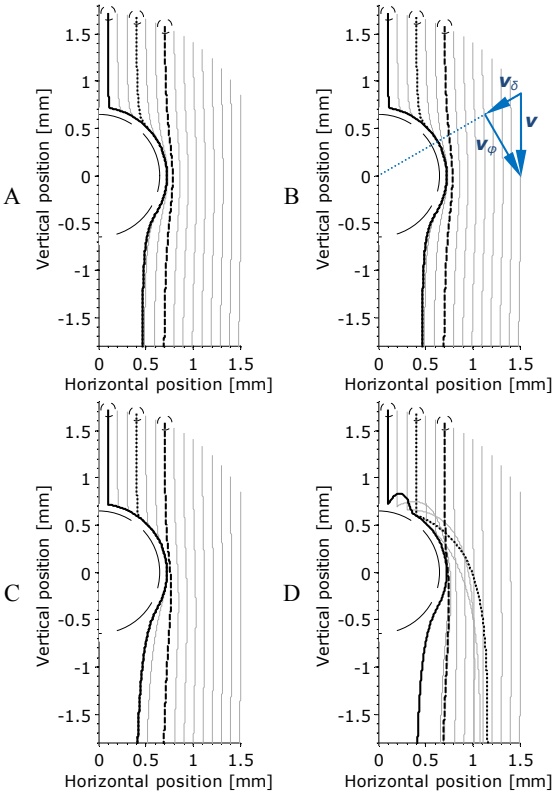

Figure 2: Trajectories for the four cases described in Table 2. The dashed outline indicates the bubble's surface, while the dotted outlines denote the particles. Trajectories a, b & c (Table 3) are shown as darker lines. In B the radial and tangential components of a velocity vector are also illustrated.

Figure 3: Sequence of images illustrating a spherical ~125 µm particle (soda–lime glass *Ballotini*) rebounding from the surface of a ~2.0 mm bubble. Particles were ejected from a pipette with a high velocity. The particle's movement means only a bright spot shows up at its centre (the particle focuses light from behind). The interval between successive frames is 40 ms, and the exposure time is slightly shorter.

Induction periods

The induction periods for each case are shown in **Figure 4**. All graphs share the common property that the induction period increases as the starting position of the particle moves away from the axis. This extends the findings presented previously (Verrelli *et al.*, 2012b), which corresponded only to Case A of the present work, and demonstrates general applicability of the behaviour. Predicted values are in the same range as those found experimentally.

It is interesting to observe that cases A and B show indistinguishable induction periods in **Figure 4**. The relative discrepancy between the two cases does not

exceed ±0.3 %, and indeed this is an overestimate of the true discrepancy (an artefact of the position of the data points relative to the threshold gaps). The reason for the similarity is the mass of the low-density particle is insufficient to maintain the higher initial velocity against the drag effects, and the particle in case B is decelerated to match case A before it gets to the first gap threshold of 0.001 mm. The Stokes velocities by equation 4 are a factor of 4.55 times smaller in cases A & B than in cases C & D, meaning that in the former case there is more time for the deceleration to occur, given that the distance between the particle's starting position and the surface of the bubble is the same in all cases. This indicates that light particles will be less able to maintain the elevated velocities that can be imparted to them by turbulent eddies in an industrial flotation cell, whereas the heavier particles can take greater advantage.

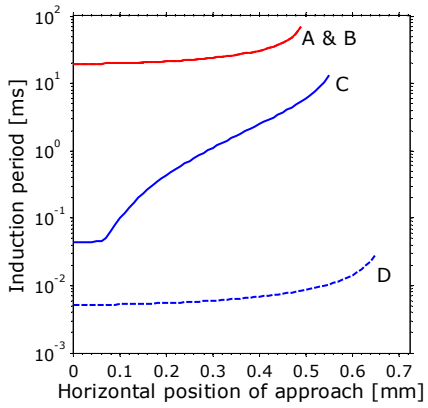

Figure 4: Inductions periods for particle–bubble attachment, for the four cases described in Table 2. The horizontal axis extends to a value of $R_b + R_p$, the theoretical limit for which attachment could occur.

Gap and force components

Gaps and force components for various conditions are shown overleaf.

In **Figure 5** the results for trajectory a of case A are shown. In the uppermost plot, the gap is seen to decrease rapidly. Attachment is expected to occur for this trajectory, under chemically favourable conditions. If the chemistry is unfavourable, the model predicts sliding on the bubble's upper hemisphere at a constant separation, followed by withdrawal once the particle centre has passed the bubble's equator.

This plot demonstrates that it is the hard-sphere repulsion term that has introduced asymmetry into the particle trajectories, because it only constrains decreases in the gap (as for $\varphi < 90°$), not increases (as for $\varphi > 90°$).

As the particle circumnavigates the bubble, the buoyancy vector gradually varies from acting toward the bubble centre, to acting parallel with the local bubble surface, to acting away from the bubble centre. This is evident in the second and third plots of **Figure 5**. In the second plot, we also see that the importance of radial Stokes drag decreases as the velocity drops (*cf.* equation 4), whereas the radial microhydrodynamic drag rapidly becomes important with the reduction in separation, only reducing back to zero when another force arises to prevent the radial motion.

The relatively slow 'sliding' speed means that the tangential Stokes drag is also small, as seen in the third plot. In contrast, the tangential microhydrodynamic drag is the main force balancing the tangential component of buoyancy force, given the small gap. Both the radial and tangential $F_{i,\mathrm{IAM}}$ terms remain quite small throughout for this trajectory.

In **Figure 6** we see that when the horizontal offset of the particle's initial position increases, the gap decreases more slowly due to the geometry; this results in a smaller radial velocity, which yields a longer induction period according to our specified thresholds.

In **Figure 7** the particle is not able to reach even the threshold for sliding, as the microhydrodynamic drag acts at relatively long range, causing the particle to deviate from its original path while still quite far from the bubble, as shown in **Figure 2**. Here the induction time for attachment is 'infinite', or undefined.

Figure 8 shows the radial force components only for trajectory a of case B. It is apparent that the velocity which is initially $4\boldsymbol{v}_S$ decreases almost immediately — within approximately 15 ms the particle speed has reduced to the same value as the particle in case A. Hence, after the first few milliseconds the forces are very similar between cases A & B, as evident by comparison with **Figure 5**. This also simplifies the modelling of particle–bubble interactions for this class of particle, as it suggests that the complications of high inertia (or high Reynolds number) are minor effects.

In **Figure 9** the gap and force components are shown for one of the heavy-particle scenarios (trajectory b, case C). This exhibits a fascinating feature beginning at $\delta \sim 56$ nm, in which the rate of change of the gap suddenly changes its form. It must be emphasised that this feature is totally unrelated to the threshold for determining attachment (10 nm), which is a *post hoc* analysis, and is not at all influenced by the hard-sphere repulsion term, which would contribute a force of $(1/53)^{200} m_p$ N $\approx 2\times10^{-344}$ nN — vanishingly small. Rather, it is a natural feature due to a combination of geometry and the forms of the microhydrodynamic drag functions.

Examining the force components in **Figure 9** reveals that there is a 'runaway' spike in the microhydrodynamic resistances leading up to this event. At the same time, there is a drastic slowing of the particle, for $30° < \varphi < 35°$, coinciding with a conversion from mostly radial motion to almost entirely tangential motion (or energy). This suggests that these energetic interactions are pushing the limit of applicability of the present numerical model. Although the model does include inertial and added mass terms in the governing equation, it neglects the Basset force, which is important when significant accelerations or decelerations occur (Clift *et al.*, 1978). Furthermore, the microhydrodynamic drag functions (and indeed Stokes equation) were derived for creeping flow, and will become increasingly poor estimates as the contribution of inertia rises. While an inertia-corrected form of f_r is available in the limit of small gaps (Cox & Brenner, 1967), it does not rigorously handle particle acceleration or large gaps, and leaves open the question of how to handle f_t; a numerical simulation of the full flow field based on the Navier–Stokes equations is the recommended approach.

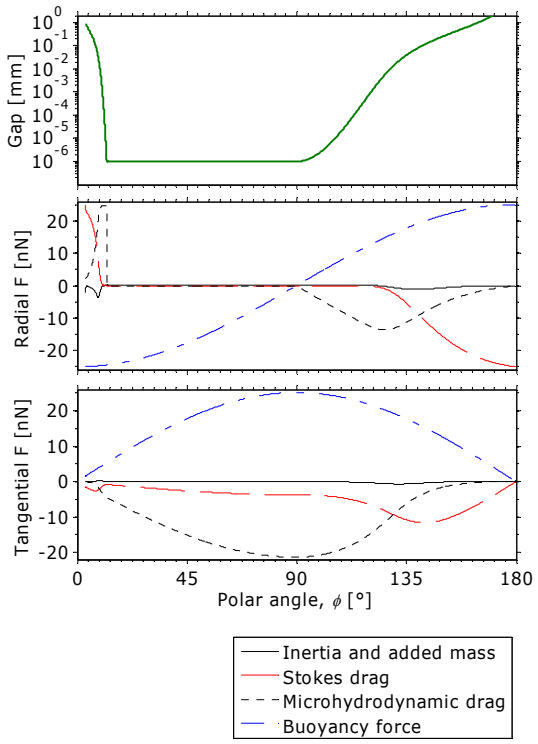

Figure 5: Gap and force components for trajectory a (see Table 3) of case A (see Table 2).

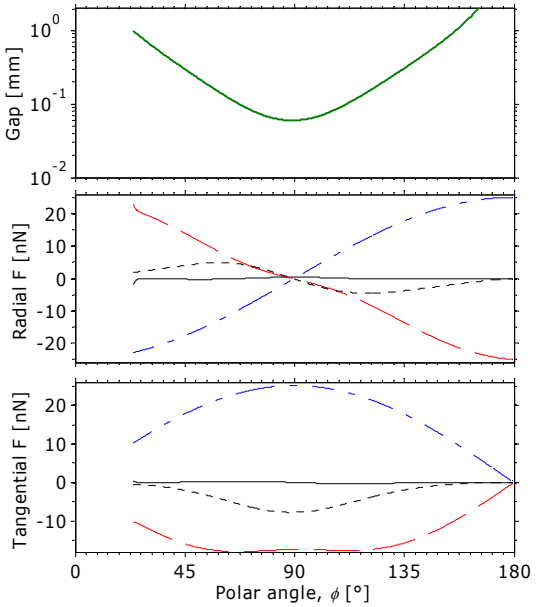

Figure 7: Gap and force components for trajectory c of case A. Legend as in Figure 5.

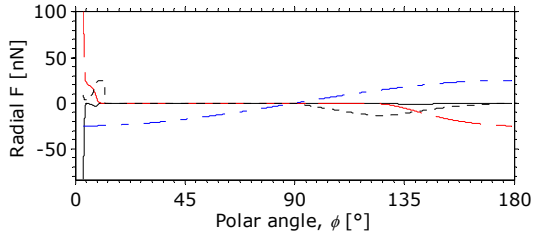

Figure 8: Radial force components for trajectory a of case B. Legend as in Figure 5.

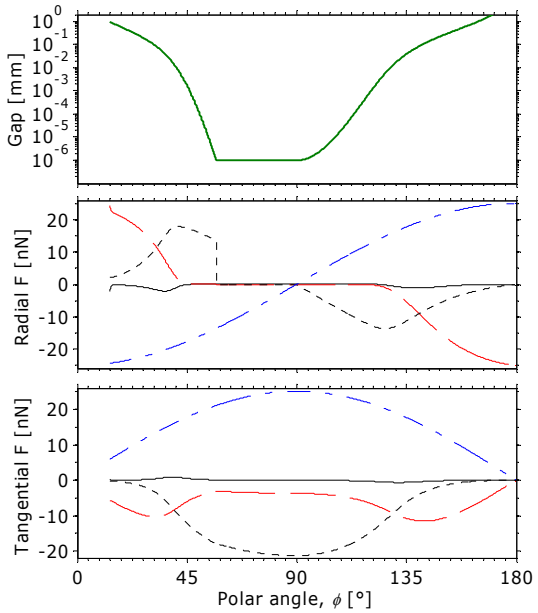

Figure 6: Gap and force components for trajectory b of case A. Legend as in Figure 5.

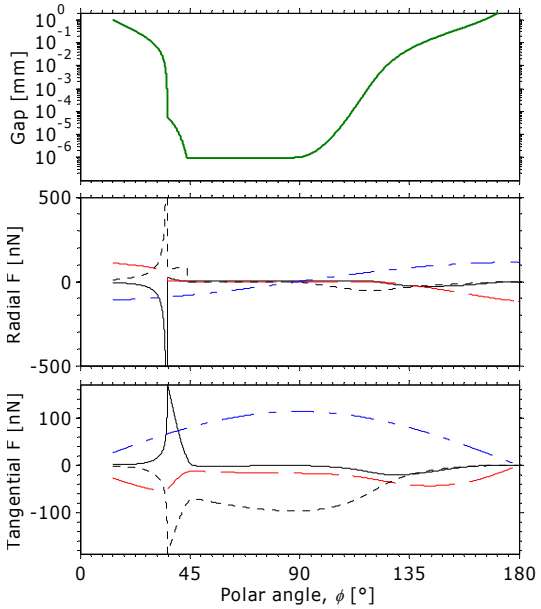

Figure 9: Gap and force components for trajectory b of case C. Legend as in Figure 5. The radial microhydrodynamic drag spikes at just over 5000 nN, while the inertia & added mass term spikes down to just under −5000 nN.

Although not shown here, the inertia & added mass terms are even greater in case D, as expected. Notably, as expected from a comparison of the trajectories or induction periods, the greater density of the particles in cases C & D has meant that the elevated initial velocity was able to be maintained long enough to have major effects on the behaviour. In case D, even more concern is raised as to the necessity of extending the numerical models out of the creeping flow regime.

CONCLUSION

The present work has shown the importance of detail in modelling bubble–particle interactions for applications such as industrial froth flotation. For the lighter particles examined, the effect of quadrupling the initial approach velocity was negligible, but it had a significant effect on the response of the heavier particles.

Inclusion of a hard-sphere repulsion term introduced a distinct asymmetry to the particle trajectories for nonattaching particles. For the most energetic particles 'bouncing' on the bubble's surface was predicted if a chemical repulsion prevented attachment, whereas less energetic particles 'slide' off the bubble. This is consistent with our experimental observations.

The conclusion that the induction period cannot be assumed constant has been extended to a range of particle densities and initial velocities. Up to now this feature has not been appropriately considered in the general flotation literature.

Extracting values of the individual force components has provided greater insight into the mechanisms influencing the particle's behaviour as it interacts with the bubble. Examining these forces also provides information on the range of validity of the governing equations, boundary conditions, and assumptions made in the modelling. It was seen that for particles at the larger and heavier end of the spectrum encountered in industrial flotation operations, the acceleration and inertial contributions could be significant, or even dominant, and the present analytical formulæ are unable to rigorously handle such conditions.

ACKNOWLEDGEMENTS

We give credit to Prof. Anh Nguyen for formulating the original algorithms used in our *Chem. Eng. Sci*. paper. We gratefully acknowledge the ongoing support of CSIRO's Advanced Scientific Computing team, with special thanks to Dr. Tim Ho. *MediaCoder* from Stanley Huang, *VirtualDub* from Avery Lee, and *IrfanView* from Irfan Skiljan were used to process the video. We acknowledge Prof. George Franks for coordinating A. Lee's involvement in this work. We also appreciate Mr. Warren Bruckard's ongoing support. Finally, we thank CSIRO Process Science and Engineering for funding the work.

APPENDIX

Values of the coefficients C_i and D_i used in equations 6 and 7 are provided in **Table 5**.

i	C_i	D_i
1	13.6452247722458	0.1292257552759118
2	75.9063050402686	4.281129177286589
3	491.854093164041	7.806735049853723
4	-310.053937216871	5.349521744657736
5	5474.15594699018	1.304938272355011
6	-4855.17486956623	0.9939520955286008
7	8183.99690490305	
8	-1907.24186920391	
9	1259.36564512760	
10	51.4351824486848	
11	24.4862595399736	

Table 5: Values of the coefficients C_i and D_i.

REFERENCES

CHAOUI, M. & FEUILLEBOIS, F., (2003), "Creeping flow around a sphere in a shear flow close to a wall", *The Quarterly Journal of Mechanics and Applied Mathematics*, **56**(3), 381–410.

CLIFT, R., GRACE, J.R. & WEBER, M.E., (1978), *Bubbles, Drops, and Particles*, Academic Press, New York, U.S.A.

COX, R.G. & BRENNER, H., (1967), "The slow motion of a sphere through a viscous fluid towards a plane surface—II. Small gap widths, including inertial effects", *Chemical Engineering Science*, **22**(12), 1753–1777.

LIU, T.Y. & SCHWARZ, M.P., (2009), "CFD-based multiscale modelling of bubble–particle collision efficiency in a turbulent flotation cell", *Chemical Engineering Science*, **64**(24), 5287–5301.

NEWCOMBE, B., (2009), "An operators' guide to sulfide mineral flotation", *Tenth Mill Operators' Conference 2009*, The Australasian Institute of Mining and Metallurgy, Carlton, Victoria, Australia, Adelaide, South Australia, 211–221.

NGUYEN, A.V. & EVANS, G.M., (2004), "Exact and global rational approximate expressions for resistance coefficients for a colloidal solid sphere moving in a quiescent liquid parallel to a slip gas–liquid interface", *Journal of Colloid and Interface Science*, **273**(1), 262–270.

NGUYEN, A.V. & SCHULZE, H.J., (2004), *Colloidal Science of Flotation*, Marcel Dekker, New York, U.S.A.

SCHULZE, H.J. & GOTTSCHALK, G., (1981), "Investigations of the hydrodynamic interaction between a gas bubble and mineral particles in flotation", in: LASKOWSKI, J.S. (Ed.), *Thirteenth International Mineral Processing Congress*, Elsevier Scientific, Amsterdam, The Netherlands / PWN, Warsaw, Poland, Warsaw, 04–09 June 1979, Part A, pp. 63–85.

SHAMPINE, L.F. & REICHELT, M.W., (1997), "The MATLAB ODE suite", *SIAM Journal on Scientific Computing*, **18**(1), 1–22.

SVEN-NILSSON, I., (1934), "Einfluß der Berührungszeit zwischen Mineral und Luftblase bei der Flotation", *Kolloid Zeitschrift*, **69**(2), 230–232.

VERRELLI, D.I. & KOH, P.T.L., (2010), "Understanding particle–bubble attachment: experiments to improve flotation modelling", *Chemeca 2010*, IChemE in Australia / EA / RACI / SCENZ-IChemE N.Z., Adelaide, Australia.

VERRELLI, D.I., KOH, P.T.L. & NGUYEN, A.V., (2011), "Particle–bubble interaction and attachment in flotation", *Chemical Engineering Science*, **66**(23), 5910–5921 & Supplementary Material.

VERRELLI, D.I., (2012), "Localised inducement of bubble surface mobility due to motion of a nearby particle", in: WITT, P.J. (Ed.), *Ninth International Conference on Computational Fluid Dynamics in the Minerals and Process Industries (CFD2012)*, CSIRO, Australia, Melbourne, Australia, Submitted.

VERRELLI, D.I., BRUCKARD, W.J., KOH, P.T.L., SCHWARZ, M.P. & FOLLINK, B., (2012a), "Influence of particle shape and roughness on the induction period for particle-bubble attachment", in: RUNKANA, V. & RAI, B. (Eds.), *XXVI International Mineral Processing Congress (IMPC 2012)*, Indian Institute of Mineral Engineers (IIME) and Indian Institute of Metals (IIM), New Delhi, India.

VERRELLI, D.I., KOH, P.T.L., BRUCKARD, W.J. & SCHWARZ, M.P., (2012b), "Variations in the induction period for particle–bubble attachment", *Minerals Engineering*, **accepted March 2012** (http://dx.doi.org/10.1016/j.mineng.2012.03.034).

